Spatiotemporal transcriptional dynamics of the cycling mouse oviduct

Elle C. Roberson[1], Anna M. Battenhouse[1], Riddhiman K. Garge[1], Ngan Kim Tran[1], Edward M. Marcotte[1], John B. Wallingford[1,*]

[1]Department of Molecular Biosciences, University of Texas at Austin, TX, USA 78712

ORCID: ECR, orcid.org/0000-0001-7466-7447; AMB, orcid.org/0000-0002-7455-9064; RKG, orcid.org/0000-0002-6774-0172; EMM, orcid.org/0000-0001-8808-180X; JBW, orcid.org/0000-0002-6280-8625

[*]Corresponding author information:
wallingford@austin.utexas.edu
Patterson Labs
University of Texas at Austin
2401 Speedway
Austin, TX 78712

Abstract

Female fertility in mammals requires iterative remodeling of the entire adult female reproductive tract across the menstrual/estrous cycle. However, while transcriptome dynamics across the estrous cycle have been reported in human and bovine models, no global analysis of gene expression across the estrous cycle has yet been reported for the mouse. Here, we examined the cellular composition and global transcriptional dynamics of the mouse oviduct along the anteroposterior axis and across the estrous cycle. We observed robust patterns of differential gene expression along the anteroposterior axis, but we found surprisingly few changes in gene expression across the estrous cycle. Notable gene expression differences along the anteroposterior axis included a surprising enrichment for genes related to embryonic development, such as Hox and Wnt genes. The relatively stable transcriptional dynamics across the estrous cycle differ markedly from other mammals, leading us to speculate that this is an evolutionarily derived state that may reflect the extremely rapid five-day mouse estrous cycle. This dataset fills a critical gap by providing an important genomic resource for a highly tractable genetic model of mammalian female reproduction.

Introduction

The adult mammalian female reproductive organs – ovary, oviduct, uterus, cervix, and vagina – hold an interesting position in mammalian physiology because they constantly and repeatedly engage in a complex remodeling process more commonly associated with development. With every menstrual or estrous cycle, fluctuations in ovarian steroid hormone secretion drive remodeling of these tissues, characterized by changes in proliferation, apoptosis, epithelial morphology, and fluid secretion (Brenner and West, 1975). However, while decades of research have revealed how these hormones fluctuate across the menstrual/estrous cycle in multiple mammals, we understand far less about the mechanisms by which these hormones drive cyclic tissue morphogenesis.

The oviducts are most well-known as the conduit between the ovary and uterus, but it is critical to note they also function as the site of fertilization and pre-implantation embryonic development (Coy et al., 2012; Coy and Yanagimachi, 2015; Stewart and Behringer, 2012). Interestingly, the oviducts display robust patterning along the anteroposterior axis, as the two major epithelial cell types – multiciliated cells (MCCs) and secretory cells – are differentially

32   enriched (Agduhr, 1927; Barton et al., 2020; Stewart and Behringer, 2012). At the anterior

33   oviduct close to the ovary, MCCs are highly enriched and responsible for capturing the ovulated

34   oocyte(s), while at the posterior close to the uterus, MCCs are very sparse and act as sperm

35   reservoirs (Suarez, 2016; Talbot et al., 1999). The reduced proportion of MCCs in the posterior

36   oviduct reflects the significant increase in the proportion of secretory cells, which are critical to

37   pre-implantation development (Coy and Yanagimachi, 2015). This anteroposterior pattern of the

38   mouse oviduct epithelium is known to be established early in postnatal life and requires signaling

39   from the underlying mesenchyme (Yamanouchi et al., 2010). How this pattern may change

40   across the estrous cycle is not known.

41   In many species, the cellular basis of morphogenesis of oviduct MCCs across the estrous

42   cycle was described *via* scanning electron microscopy studies decades ago (Brenner, 1969;

43   Shirley and Reeder, 1996; Verhage et al., 1973). In Rhesus monkeys, for example, anterior

44   oviduct epithelial cells are cuboidal at the beginning of the cycle, but then grow in height and

45   develop cilia at their apical surfaces as estrogen increases (Brenner, 1969). As estrogen decreases

46   and progesterone increases, the MCCs regress and de-ciliate (Brenner, 1969).

47

48   In mice, however, such cellular changes have not been thoroughly investigated, although

49   it was shown that the wet weight of oviducts, as well as RNA and protein concentration,

50   increases in the first half of the estrous cycle, and then subsequently decreases during the second

51   half (Bronson and Hamilton, 1971; Yamanouchi et al., 2010). More recently, there is evidence

52   that ciliary beat frequency changes in response to estrogen and progesterone (Bylander et al.,

53   2010; Shi et al., 2011). Perhaps surprisingly, while steroid hormone signaling in the oviduct is

54   crucial for female fertility (Herrera et al., 2020; Winuthayanon et al., 2015), we still lack a

55   comprehensive view of how cycling steroids impact cellular morphogenesis in the oviduct,

56   especially in the mouse.

57   A major hurdle to filling this knowledge gap is our very limited understanding of the

58   transcriptional dynamics that underlie cyclical morphogenesis in this tissue. Transcriptomic

59   approaches in human, swine, and bovine oviducts have investigated the impact of estrogen and

60   progesterone, and some studies have also explored anteroposterior patterning in humans and

61   bovine oviducts (Bauersachs et al., 2004; Cerny et al., 2015; Hess et al., 2013; Kim et al., 2018;

62   Sowamber et al., 2020). However, the majority of these studies have focused on either the

63 transcriptional response to fertilization and early embryo development or transcriptional

64 signatures associated with progression of high grade serous ovarian carcinoma in the oviduct.

65 The absence of a dynamic mouse oviduct transcriptome across the normal estrous cycle

66 represents a critical gap in our knowledge, especially given its potential utility as a model for

67 understanding mammalian fertility.

68 Here, we examined both the cellular changes and global transcriptional dynamics along

69 the length of the oviduct and across the estrous cycle. First, we provide quantitative data on the

70 density of MCCs along the anteroposterior axis of the oviduct and we show that MCCs do not

71 remodel across the estrous cycle in mice. In addition, we present 3' RNA-seq (Lohman et al.,

72 2016) data for the anterior (approximate infundibulum) and posterior (approximate isthmus)

73 oviduct at each stage of the estrous cycle. While transcript abundances vary strongly along the

74 anteroposterior axis, our analyses suggest the estrous cycle has a surprisingly limited impact on

75 transcription. Our data complement previous studies of transcriptional dynamics in the oviduct of

76 other mammals and provide an important new resource for genetic studies of oviduct function in

77 the mouse.

78

79 **Materials and Methods**

80 *Mice*. 6-8-week-old Swiss Webster female mice were obtained from Charles River and allowed

81 to acclimate from travel for 1 week. Mice were housed in individually ventilated cages in a

82 pathogen-free facility with continuous food and water, with a controlled light cycle (light from

83 7am-7pm). 7-9-week-old females were estrous cycle staged using standard vaginal cytology

84 (Ajayi and Akhigbe, 2020). Mice were humanely euthanized with extended CO_2 exposure

85 followed by cervical dislocation, and female reproductive tracts were dissected. All animal

86 experiments were approved by the University of Texas at Austin Institutional Animal Care and

87 Use Committee.

88

89 ***Tissue processing & immunofluorescence***. Dissected oviducts were carefully linearized (Fig.

90 1A) by teasing apart the supercoils, gently affixing to a strip of index card to keep the tissue

91 straight, then fixing in 4% paraformaldehyde for either 4-6hr at room temperature (RT) or

92 overnight at 4°C. Linearized fixed oviducts were washed in PBS, and then incubated in 30%

93 sucrose at 4°C overnight. Following a brief incubation in NEG-50 Frozen Section Medium

94   (ThermoFisher), oviducts were embedded in NEG-50 using an ethanol/dry ice bath. 12μm frozen

95   longitudinal sections were cut on a cryostat (Leica) and dried overnight at RT. Frozen sections

96   were stored at -20°C.

97   Tissue sections were washed in PBS + 0.1% Tween20 (PBST) three times to remove

98   NEG-50. Tissues were blocked for at least 30min at RT with 5% normal donkey serum + PBS

99   (block buffer). Primary antibodies for cilia (mouse anti-acetylated tubulin, 1:1000 dilution,

100   Sigma, cat# 6-11B-1) were diluted in block buffer and incubated on slides for 2hr at RT or

101   overnight at 4°C. After washing three times with PBST, slides were incubated with Alexa-Fluor

102   coupled secondary antibodies (goat anti-mouse 647, 1:1000 dilution, ThermoFisher) and DAPI

103   (1:1000 dilution, ThermoFisher) for at least 30min at RT. After washing, slides were mounted

104   with Prolong Gold (ThermoFisher), and allowed to cure at RT in the dark overnight. Oviduct

105   sections were imaged on either a Zeiss LSM700 point scanning confocal microscope or a CSU-

106   W1 spinning disk Nikon confocal.

107

108   ***Tissue sectioning and quantitation***. Two to four sections spaced at least 100μm apart were

109   analyzed for cilia at four locations along the anteroposterior axis of the oviduct. Images from the

110   the fimbria, anterior third (approximate infundibulum), middle third (approximate ampulla), and

111   posterior third (approximate isthmus) were acquired and quantified. We quantified ciliary area as

112   previously published (Roberson et al., 2020). Briefly, we used FIJI image processing to trace the

113   lumen based on DAPI staining to approximate the luminal length. Similarly, the ciliated surface

114   of the lumen was traced and measured based on acetylated tubulin staining. From these

115   measurements, the % ciliated surface area was calculated for each image, and we plotted using

116   GraphPad Prism 8.

117

118   ***RNA isolation and cDNA synthesis.*** For 3' TagSeq (see below), dissected oviduct samples were

119   collected in duplicate for each of the four stages across both anterior and posterior regions. For

120   qPCR, samples were collected in triplicate for each estrous cycle stage across anterior, middle,

121   and posterior thirds of the mouse oviduct. Following storage in RNA*Later* Storage Solution

122   (Sigma, cat#: R0901) at -20°C, oviduct tissue was manually disrupted and the lysate was spun

123   through a QIAshredder column (Qiagen, cat#: 79656) to fully homogenize. A Qiagen RNeasy

124   mini kit (Qiagen, cat#: 74106) was used to harvest RNA for RNAseq, and the Qiagen RNeasy

5

125 micro kit (Qiagen, cat#: 74004) was used to harvest RNA for qPCR. Total RNA was then either

126 provided to the Genomic Sequencing and Analysis Facility at the University of Texas at Austin

127 for 3' TagSeq, or cDNA was synthesized using the iScript Reverse Transcription SuperMix

128 (BioRad, cat#: 1708841) for qPCR.

129

130 *qPCR.* Most primers were designed from a database for mouse and human qPCR primers

131 incorporated into the UCSC genome browser (Zeisel et al., 2013). Primers for *Foxj1* and *Msx2*

132 were designed using Primer3Plus software. See Supplemental Table S-1 for primer details. We

133 confirmed specificity of primers by ensuring that they BLAST to no more than 1 site in the

134 genome. There were four outliers to this BLAST assessment: all four ribosome primer sets

135 blasted to more than 1 site in the genome, likely because there are numerous ribosomal

136 pseudogenes scattered throughout the genome (Sisu et al., 2020). In addition, we only used

137 primers whose melting curve displayed a single peak.

138 Primer sets were diluted from a stock (100μm in TE buffer) to 1μM in distilled deionized

139 H$_2$O. 2μL of each primer set (in technical duplicates) was allowed to dry in the bottom of a well

140 in a MicroAmp Fast Optical 96 Well Reaction Plate (Thermofisher, cat#: 43-469-06). 10μL of a

141 master mix of cDNA (250pg/well), Applied Biosystems SYBR Select Master Mix

142 (Thermofisher, cat#: 44-729-18), and distilled deionized water was added to each well, the plates

143 were sealed with MicroAmp Optical Adhesive Film (Thermofisher, cat#: 43-119-71) and

144 allowed to incubate at RT in the dark for at least 15min to rehydrate primer. Plates were run on a

145 ViiA-7 Real-Time PCR system (ThermoFisher), and CT values were auto-determined by the

146 ViiA-7 software. The standard $2^{-\Delta\Delta Ct}$ method was then used to determine fold change based on

147 the geomean of three 'housekeeping' genes (*Hprt*, *Dolk*, and *Sra1*) (Schmittgen and Livak,

148 2008).

149

150 *TagSeq.* Tissue samples were collected in duplicate for each of the four estrous stages across

151 both anterior and posterior regions of the mice oviduct, accounting for 16 samples in total.

152 Library preparation and sequencing for TagSeq (Lohman et al., 2016; Meyer et al., 2011), a form

153 of 3' RNA sequencing, were performed by the Genomic Sequencing and Analysis Facility

154 (GSAF) at The University of Texas at Austin. Total RNA was isolated from each sample by

155 addition of Trizol (Thermo Fisher) and the sample was transferred to a Phasemaker tube

6

156   (Thermo Fisher). Total RNA was extracted following the protocol supplied by the manufacturer

157   and further cleaned up using a RNeasy MinElute Cleanup Kit (Qiagen). RNA integrity number

158   (RIN) was measured using an Agilent Bioanalyzer and 100 ng of RNA was used for the TagSeq

159   protocol. The fragmentation/RT mix was prepared and added to each RNA sample, then heated

160   to 95°C for 2.5 minutes on a Thermocycler and immediately put on ice for 2 minutes. After

161   cooling and addition of the template switching oligo and SmartScribe RT, the fragmented RNA

162   reaction was incubated at 42°C for 1hr, 65°C for 15 min. Next an AmPure bead clean-up was

163   completed for the cDNA before it was amplified to incorporate the Illumina sequencing primer

164   site, followed by another cleanup. The remaining portions of the Illumina adapter (the i5 and i7

165   indices) were then added through an additional 4 cycles of PCR. Final libraries were quantified

166   with PicoGreen then pooled equally for size selection using the Blue Pippin from 355-550 bp.

167   Resulting libraries were sequenced using an Illumina HiSeq 2500 instrument (50-nt single

168   reads). Full sample dataset details are provided in Supplemental Table S-2.

169

170   ***Sequence data pre-processing.*** Fastq datasets were initially processed to collapse duplicates

171   based on TagSeq molecular barcodes (Matz). Sequencing data quality, both before and after

172   TagSeq pre-processing, was evaluated using the FastQC tool (v0.11.9) (Andrews) and reports

173   were aggregated with the MultiQC program (v1.0) (Ewels et al., 2016).

174

175   ***TagSeq data analysis.*** Single-end pseudo-alignment was performed against the mouse

176   transcriptome (GENCODE M23 transcript sequences (Frankish et al., 2019)) using kallisto

177   (v0.45.0) (Bray et al., 2016) with options -l 200 -s 50 --single-overhang –bias. Downstream

178   analysis of transcript abundance data was performed in R (v3.4.4) following protocols outlined

179   in Bioconductor (Gentleman et al., 2004). The tximport package (v1.6.0) (Soneson et al., 2015)

180   was first used to roll up transcript-level counts into gene-level counts provided to

181   the DESeq2 package (v1.18.1) (Love et al., 2014). Before further analysis, count data matrices

182   were filtered to remove genes with fewer than 1 read across all included samples. A number of

183   models were analyzed to explore the oviduct location/estrous stage relationship: Posterior versus

184   Anterior locations, first providing Early and Late data separately (n=8 each), then again

185   providing all datasets (n=16); and Late versus Early, first providing Anterior and Posterior

186   location data separately (n=8 each), then again providing all datasets (n=16). Differentially

187 expressed gene results reported are those with maximum adjusted p-value 0.05 and log2 fold

188 change greater than 1.0 or less than -1.0.

189   Gene ontology (GO) analysis was performed using topGO R package (v2.34.0) (Alexa,

190 2020) with GO database org.Mm.eg.db (v3.7.0). The topGO classic algorithm and Fisher's exact

191 test were used in count data mode. Input genes had maximum adjusted p-values of 0.10. Separate

192 analyses were performed for up-regulated (log2 fold change 0.5 or higher) and down-regulated

193 (log2 fold change -0.5 or lower) genes. The background gene universe consisted of observed

194 genes used in the DESeq2 analysis.

195 Full DESeq2 and topGO results are provided in the supplementary zip file for GEO accession

196 number GSE164718.

197

198 **Results and Discussion**

199 ***Quantification of multiciliated cell density in the cycling mouse oviduct.***

200   Oviducts in most mammals consist of two key epithelial cell types – secretory and

201 multiciliated cells (MCCs) – and these are unevenly distributed across the anteroposterior axis.

202 MCCs are enriched anteriorly and secretory cells, posteriorly (Agduhr, 1927; Yamanouchi et al.,

203 2010). While dynamic morphology changes across the estrous cycle have been described in the

204 oviducts of many mammals (Brenner, 1969; Ferenczy et al., 1972; Novak and Everett, 1928;

205 Shirley and Reeder, 1996; Verhage et al., 1973), the issue has not been investigated thoroughly

206 in the mouse. To stringently assess cellular remodeling of the anteroposterior axis of the mouse

207 oviduct across the estrous cycle, we linearized the normally supercoiled oviduct by carefully

208 teasing apart each coil along the length of the organ (Fig. 1A), and generated longitudinal

209 sections of linearized tissue. We then performed immunostaining for acetylated tubulin (Tub[Ac])

210 to label MCC cilia, and DAPI to label nuclei (Fig. 1B-E).

211   By examining fimbria, anterior (approximate infundibulum), middle (approximate

212 ampulla), and posterior (approximate isthmus) regions of the oviduct, we clearly observed the

213 anterior bias in MCC density (Fig. 1B-E). We quantified this pattern by calculating the

214 percentage of cilia that line the oviduct lumen, based on Tub[Ac] staining as described previously

215 (Roberson et al., 2020) (Fig. 1F).

216   By performing parallel analyses on linearized oviducts from each stage of the estrous

217 cycle, we found that this pattern displayed no temporal changes, with the anterior oviduct being

8

218 significantly enriched for MCCs at all stages (Fig. 1F). The absence of significant remodeling of

219 MCCs across the estrous cycle in the mouse oviduct presents a marked contrast to other

220 mammals (Brenner, 1969; Shirley and Reeder, 1996; Verhage et al., 1973). We hypothesize that

221 this discrepancy may relate to the very short (4 to 5 day) mouse estrous cycle (Ajayi and

222 Akhigbe, 2020) and time required to eliminate and re-establish ciliated cells.

223

224 ***Determining spatiotemporal transcriptome dynamics in the mouse oviduct.***

225   Patterns of secretion, and bulk RNA and protein concentrations are known to change

226 during the mouse estrous cycle (Bronson and Hamilton, 1971). To ask if such changes have a

227 transcriptional basis, we performed 3' TagSeq, a high-throughput RNAseq profiling method that

228 captures and sequences the 3' ends of mRNA transcripts, enabling efficient estimation of relative

229 gene expression (Lohman et al., 2016; Meyer et al., 2011). We performed two biological

230 replicates of 3' TagSeq on isolated anterior (highly ciliated) and posterior (minimally ciliated)

231 oviducts at each stage of the estrous cycle (Fig. 2A). Principal component analysis (PCA)

232 revealed that the majority of expression differences occur along the AP axis (72% of variance),

233 while the estrous cycle accounts for much less variance (13%) (Fig. 2B).

234   The lack of strong variation across the estrous cycle was striking, so we considered that

235 our data might be underpowered to detect statistically significant trends across time (n=2 per

236 estrous cycle stage). We therefore repeated our analyses, collapsing the estrous cycle stages into

237 'Early' (proestrus and estrus) and 'Late' (metestrus and diestrus). This approach improved

238 differentiation between the major cycle phases; the majority of differentially expressed genes

239 (DEGs) were still found along the AP axis, not across the estrous cycle. For example, of the

240 1,758 DEGs enriched in the anterior oviduct, over 65% of them (1,158) were shared between

241 Early and Late phases (Fig. 2C). Similarly, of the 1,203 DEGs enriched in the posterior, 45%

242 (542) were shared between Early and Late (Fig 2D).

243   A more granular view of these data using volcano plots illustrates this finding. In the

244 anterior oviduct, we identified only 27 early and 14 late DEGs (Fig. 2E). Similarly, modest

245 enrichments were identified in the posterior, with 54 early and 40 late DEGs (Fig. 2F). The

246 magnitude of the expression changes was also modest, with the majority of DEG effect sizes

247 (absolute value of the log2 fold change) of two or less (59% of estrous cycle DEGs, vs. 44% of

248 AP DEGs). This result contrasts starkly to the transcriptional dynamics in the oviducts of other

9

249   organisms, including human, bovine, and swine, across the menstrual/estrous cycle (Bauersachs

250   et al., 2004; Cerny et al., 2015; Hess et al., 2013; Kim et al., 2018). For example, in bovine

251   anterior oviducts, 972 genes have been reported as enriched early and 597 enriched late (Cerny et

252   al., 2015), while in human anterior oviducts, 650 genes have been reported as enriched early and

253   683 enriched late (Hess et al., 2013).

254   In contrast to the muted transcriptional dynamics across the estrous cycle, we observed

255   highly robust and spatially-restricted patterns of gene expression along the AP axis of the mouse

256   oviduct. We identified 1337 genes enriched in the anterior, and 770 in the posterior early in the

257   estrous cycle (Fig. 2G). Similarly, late in the estrous cycle, 1579 genes were enriched in the

258   anterior and 975 in the posterior (Fig. 2H). Thus, our data suggest that the mouse oviduct

259   experiences relatively modest transcriptional changes as it progresses through the estrous cycle,

260   but displays robust transcriptional differences along the AP axis.

261

262   ***The mouse oviduct transcriptome is relatively stable across the estrous cycle.***

263   While our finding of modest transcriptional variation across the estrous cycle in the

264   mouse oviduct was consistent with the general lack of robust tissue remodeling, it was still

265   surprising given the impact of cycling steroid hormones on oviduct function (Barton et al.,

266   2020). To ask if the small number of DEGs we observed across time were enriched in particular

267   classes, we performed Gene Ontology (GO) analysis (Alexa, 2020) on the early versus late

268   DEGs. In the late stages, DEGs were subtly enriched for xenobiotic metabolism: xenobiotic

269   metabolic process, cellular response to xenobiotic stimulus, and xenobiotic catabolic process

270   (Supp. Fig. 1B).

271   More interestingly, DEGs in the early stages were enriched for translation-related terms:

272   peptide metabolic process, peptide biosynthetic process, translation, gene expression, and

273   cellular amide metabolic process (Supp. Fig. 1A). This enrichment for translation-related terms

274   early in the estrous cycle is consistent with the known concomitant increase in protein

275   concentration (Bronson and Hamilton, 1971). In agreement with the GO analysis, manual

276   annotation revealed an enrichment of large and small ribosome subunit genes expressed in the

277   early estrous cycle compared to late (Fig. 3A), with these genes displaying a 2 to 4-fold change

278   in abundance (Fig. 3B).

279   Further curation identified potentially interesting candidates based on their known or

280   hypothesized function in female fertility. For example, *Mki67*, *Ddit4*, *Atp1a1*, *Slc7a11*, *Mmp11*,

281   *Mmp7*, *Spock1*, and *Wsb1* were each enriched at early stages, while *Mamdc4*, *Gstp2*, *Gsta3*,

282   *Susd2*, and *Ap1g2* were enriched late, either in the anterior, posterior, or both (Fig. 3C). Among

283   these, *Mmp7* and *Slc7a11* were especially interesting, because both were upregulated early and

284   down regulated late, a pattern that is consistent with that observed in the cycling human oviduct

285   (Hess et al., 2013). *Mmp7* is part of the matrix-degrading enzyme family, and its down-

286   regulation late in the human menstrual cycle is hypothesized to help maintain oviduct matrix

287   integrity as the pre-implantation embryo travels through the organ (Hess et al., 2013). *Slc7a11* is

288   a glutamate/cysteine antiporter that is similarly regulated in the bovine oviduct (Cerny et al.,

289   2015). The majority of these DEGs also displayed modest effect sizes, similar to the ribosomal

290   genes (Fig. 3D).

291   To independently verify the observed stability of the oviduct transcriptome across the

292   estrous cycle, we performed qPCR for several of the DEGs. Consistent with the transcriptome-

293   wide data, we did not observe statistically significant changes across the estrous cycle for most

294   genes assayed (Fig. 3E-K), but the trends in expression consistently reflected trends in our

295   TagSeq data. The robust differential expression observed by qPCR between anterior and

296   posterior (see next section) indicate that these negative findings across the cycle do not reflect a

297   lack of sensitivity in our assays. Rather, we conclude that the relatively modest remodeling

298   observed in the oviduct by histology (Fig. 1) is reflected by relatively muted transcriptional

299   dynamics across the estrous cycle. While future work will be required, it seems reasonable to

300   suggest that the stability of the mouse oviduct across the estrous cycle represents an

301   evolutionarily derived state associated with the extremely rapid mouse estrous cycle, which at

302   four to five days, is much faster than in other organisms (Brenner and West, 1975).

303

304   ***The mouse oviduct displays robust transcriptional patterning along the anteroposterior axis.***

305   We next sought to understand the robust changes in gene expression we observe along

306   AP axis of the oviduct. We therefore turned again to GO Term analysis (Alexa, 2020).

307   Consistent with the strong anterior enrichment of MCCs observed by histology (Fig. 1), anterior-

308   enriched DEGs were highly enriched for cilia-related processes (Supp. Fig. 1C). In the anterior,

309   complexes that function in MCCs, including intraflagellar transport, transition zone, CPLANE,

310   and BBSome proteins (Garcia et al., 2018), as well as ciliary motility (Legendre et al., 2020) and

311   MCC transcription factors (Lewis and Stracker, 2020) were enriched (Fig. 4A). To provide

312   additional resolution to these patterns of expression for MCC-specific genes, we performed

313   qPCR for several at each estrous cycle stage, using not just anterior and posterior regions but

314   also the intervening middle region of the oviduct. We observed robust, statistically significant

315   enrichment in the anterior region for a ciliary transcription factor (*Foxj1*), a transition zone

316   complex gene (*Tmem231*), two ciliogenesis genes (*Ift140* and *Ift57*), and one gene encoding a

317   component of the ciliary beating machinery (*Dnah9*) (Fig. 4F-I).

318   To investigate whether mouse anterior oviduct DEGs are similar to human multiciliated

319   tissues, we compared our MCC-enriched dataset to the recently published human multiciliated

320   tissue transcriptional signature (Patir et al., 2020). The analysis of four human multiciliated

321   tissues, including ependymal, oviduct, trachea, and sperm, identified 248 genes expressed by all

322   four tissues. Of those, we find 166 of them to be differentially expressed in the anterior of the

323   mouse oviduct (data not shown), suggesting that, transcriptionally, multiciliated genes of the

324   mouse oviduct are highly similar to those of human multiciliated tissues.

325   Non-ciliated epithelial cells in the posterior oviduct consist predominantly of secretory

326   cells (Agduhr, 1927; Ghosh et al., 2017). Accordingly, our posterior-enriched gene set was

327   strongly enriched for transport and secretion GO Terms (Supp. Fig. 4), including solute carriers,

328   transport ATPases, Ca^{2+} and K^+ channels (Fig. 4A). These GO terms are similar to previously

329   published datasets from other mammals, including cows and humans, where vesicle-mediated

330   transport, endocytosis, and exocytosis were among the main processes enriched in the posterior

331   (Gonella-Diaza et al., 2017; Maillo et al., 2016; Rose et al., 2020). We confirmed this trend using

332   qPCR for a transport ATPase (*Atp1b1*) and a solute carrier (*Slc39a8*); both were significantly

333   enriched in the posterior (Fig. 4K, L).

334   Interestingly, certain genes enriched in the mouse oviduct posterior are differentially

335   expressed across the human menstrual cycle (Hess et al., 2013). For example, of the 33 solute

336   carrier (Slc) genes that are enriched in the posterior of the mouse oviduct, eight of them are also

337   differentially expressed across the human menstrual cycle, including *Slc2a3*, *Slc22a23*, *Slc27a3*,

338   *Slc39a14*, *Slc39a2*, *Slc39a8*, *Slc4A7*, *Slc8a1* (Hess et al., 2013). These Slc genes are

339   hypothesized to be important for secreting amino acids and other nutrients into the oviductal

340   lumen to aid in preimplantation embryonic development. Further studies investigating SLC

341 expression dynamics across both humans and mice may offer insights into the evolution of

342 mammalian reproduction and divergence underlying these secretory cell types.

343

344 ***Patterned expression of known developmental signaling systems along the anteroposterior***

345 ***axis of the adult oviduct.***

346   Our analysis of anteroposterior gene expression patterns also revealed several previously

347 unreported trends. First, the genes up-regulated specifically in the posterior oviduct were

348 strongly enriched for GO Terms related to embryonic development (Supp. Fig. 1D). For

349 example, all three non-canonical Wnt ligands, *Wnt5a*, *Wnt7a*, and *Wnt11* were enriched in the

350 posterior region of the oviduct (Fig. 4B, N, O). Moreover, two antagonists of canonical Wnt

351 signaling were also differentially expressed, but in a curious fashion: *Dkk2* was enriched in the

352 posterior, while *Dkk3* was enriched in the anterior (Fig. 4B). Components of the FGF signaling

353 pathway were also differentially expressed: *Fgf1*, *Fgf16*, and *Fgf2* were enriched in the posterior,

354 while only the FGF receptor, *Fgfr3*, was enriched in the anterior (Fig. 4C). Finally, multiple

355 transcription factors were differentially expressed, including Msx2 (Fig. 4M) and several Hox

356 genes, including *Hoxa9* and *Hoxa10* (Fig. 4D), both of which are involved in female

357 reproductive tract development (Du and Taylor, 2015). Other differentially expressed Hox genes

358 include *Hoxb2*, *Hoxb7*, *Hoxb8*, and *Hoxc10* (Fig. 4D). We confirmed the differential expression

359 of many of the developmental regulators using qPCR (Fig. 4M-O)

360   Not all signaling pathways displayed patterned expression, and an excellent example is

361 the Planar Cell Polarity (PCP) pathway (Fig. 4E). The PCP system is essential for normal

362 polarized ciliary beating in the oviduct, so most PCP genes are expressed in the oviduct (Koyama

363 et al., 2019; Shi et al., 2014). Strikingly however, none displayed enrichment along the AP axis

364 (Fig. 4E).

365   In contrast to intracellular effectors of PCP signaling, expression of non-canonical Wnt

366 ligands was strongly polarized, which was of interest for multiple reasons. First, Wnt signaling is

367 necessary to maintain stemness in human oviduct organoid cultures (Kessler et al., 2015), and

368 secretory cells are thought to be the progenitors of MCCs in the mouse oviduct. Thus, it may be

369 that posteriorly enriched Wnt signaling maintains the progenitor capabilities of posteriorly

370 enriched secretory cells (Ghosh et al., 2017). Second, *Wnt5a/7a/11* are known to orient PCP

371 signaling, providing directional cues for the apical surface of cells and driving coordinated

13

372   ciliary beating in multiciliated tissues (Butler and Wallingford, 2017; Gao et al., 2011; Koyama

373   et al., 2019; Ossipova et al., 2015). While the oviduct is planar polarized – i.e. Vangl2 localizes

374   anteriorly in oviduct epithelial cells – it is unknown where the directional cue originates (Shi et

375   al., 2016). Our data raise the possibility that posteriorly enriched *Wnt5a/7a/11* orients Vangl2

376   localization to the anterior side of the oviduct epithelium, thereby regulating ciliary flow towards

377   the posterior oviduct. Our experiments also indicate that PCP signaling components are evenly

378   expressed across the AP axis of the oviduct, While the impact of planar polarization on MCCs is

379   fairly well studied, the corresponding impact on secretory cells remains unknown.

380

381   **Conclusions**

382   In summary, our transcriptome profiling data fills a major gap in mouse oviduct investigations.

383   While confirming reports made using other methods, our detailed anteroposterior axis and

384   estrous stage analyses reveal novel gene expression patterns as well as providing a foundation for

385   further studies. Hypotheses generated from these data can inform additional explorations using

386   orthogonal methods such as single-cell sequencing and proteomics. Such studies have the

387   potential to identify specific cell types associated with expression trends observed here, as well

388   as quantifying actual cellular protein abundances which may differ from RNA expression.

389

397

398

399

400

401

Figure 1. The mouse oviduct displays anteroposterior patterning that does not change across the estrous cycle. A) A linearized mouse oviduct, where the anterior is close to the ovary and the posterior is close to the uterus. The insert shows a non-linearized supercoiled mouse oviduct (insert, arrow). Oviducts were collected at B) proestrus, C) estrus, D) metestrus, and E) diestrus, linearized, and imaged for nuclei (DAPI, magenta) and cilia (Tub^{Ac}, green) along the AP axis (fimbria, anterior, middle, and posterior). Scale bar = 100μm. F) Quantitation of the percent ciliated surface area along the oviduct lumen in each of the four estrous stages. Some error bars are too small to be seen. * = p< 0.05.
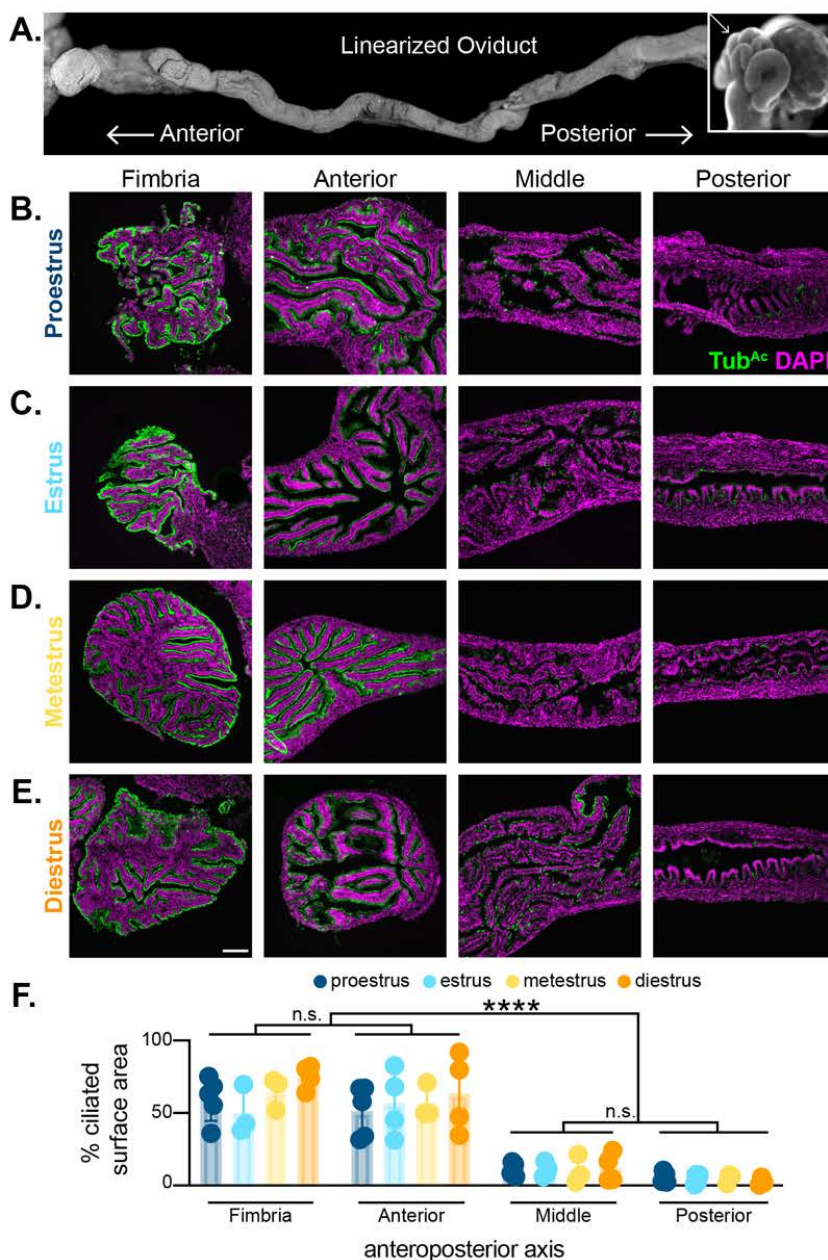
Figure 2. RNAseq of the oviduct shows major differences along the anteroposterior axis and minor change across the estrous cycle. A) Oviducts were dissected and linearized from each stage of the estrous cycle (n=2 each stage). RNA from the anterior and posterior thirds of each oviduct was collected and submitted for 3' TagSeq. B) Principal Component Analysis (PCA) of the sixteen 3'TagSeq datasets. AP location (displayed as symbols) accounts for most of the variance while estrous cycle stage (displayed as colors) accounts for a lesser part with good separation between early (Proestrus, Estrus) and late (Metestrus, Diestrus) phases. C) Overlap between the anterior DEGs at early and late estrous cycle phases. D) Overlap between the posterior DEGs at early and late phases of the estrous cycle. Volcano plots of oviduct E) anterior and F) posterior compare early and late DEGs. Volcano plots of estrous cycle G) early and H) late phases cycle show anterior and posterior DEGs. Red points are genes significant at both adjusted P-value (<= 0.05) and effect size (log2 fold change <= -1 or >= 1).
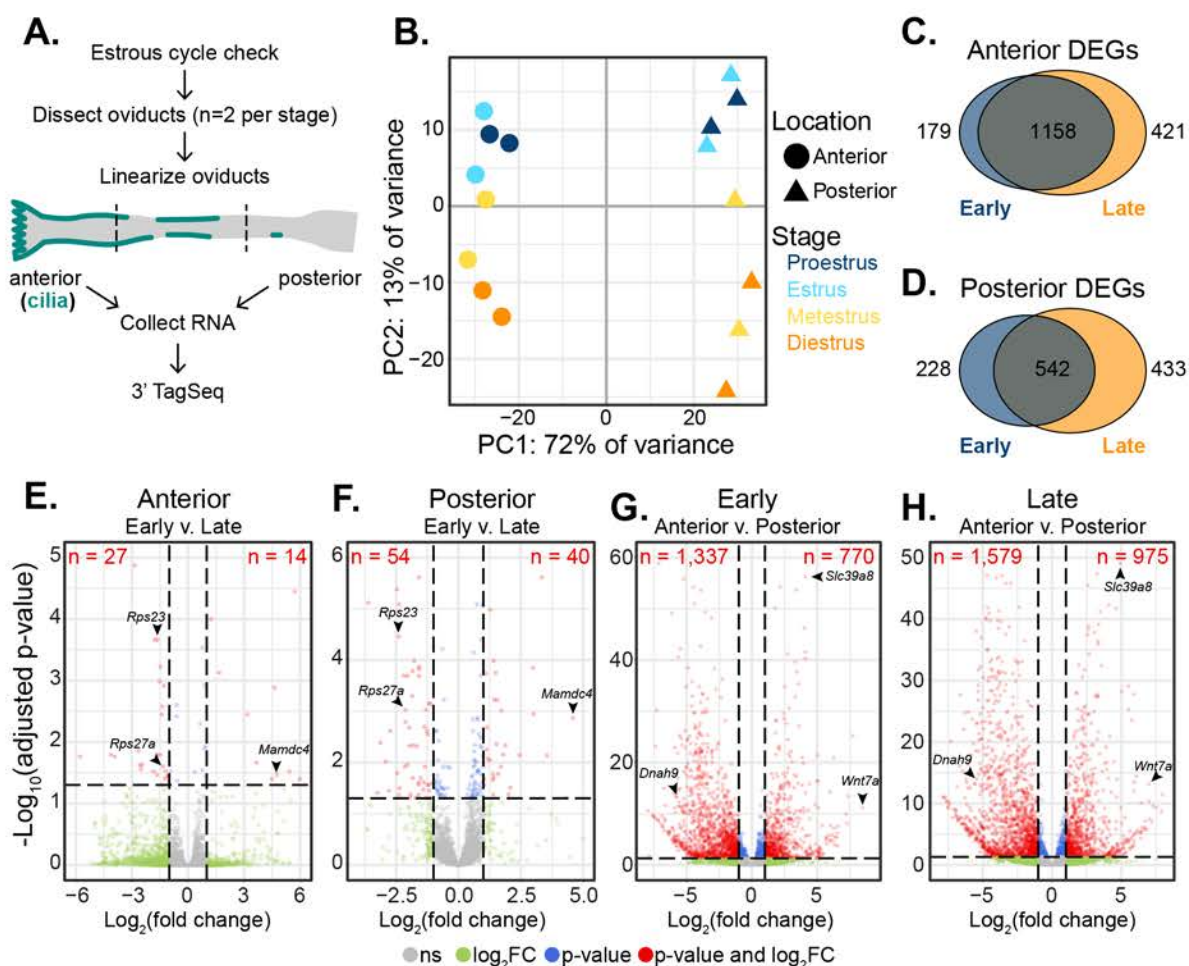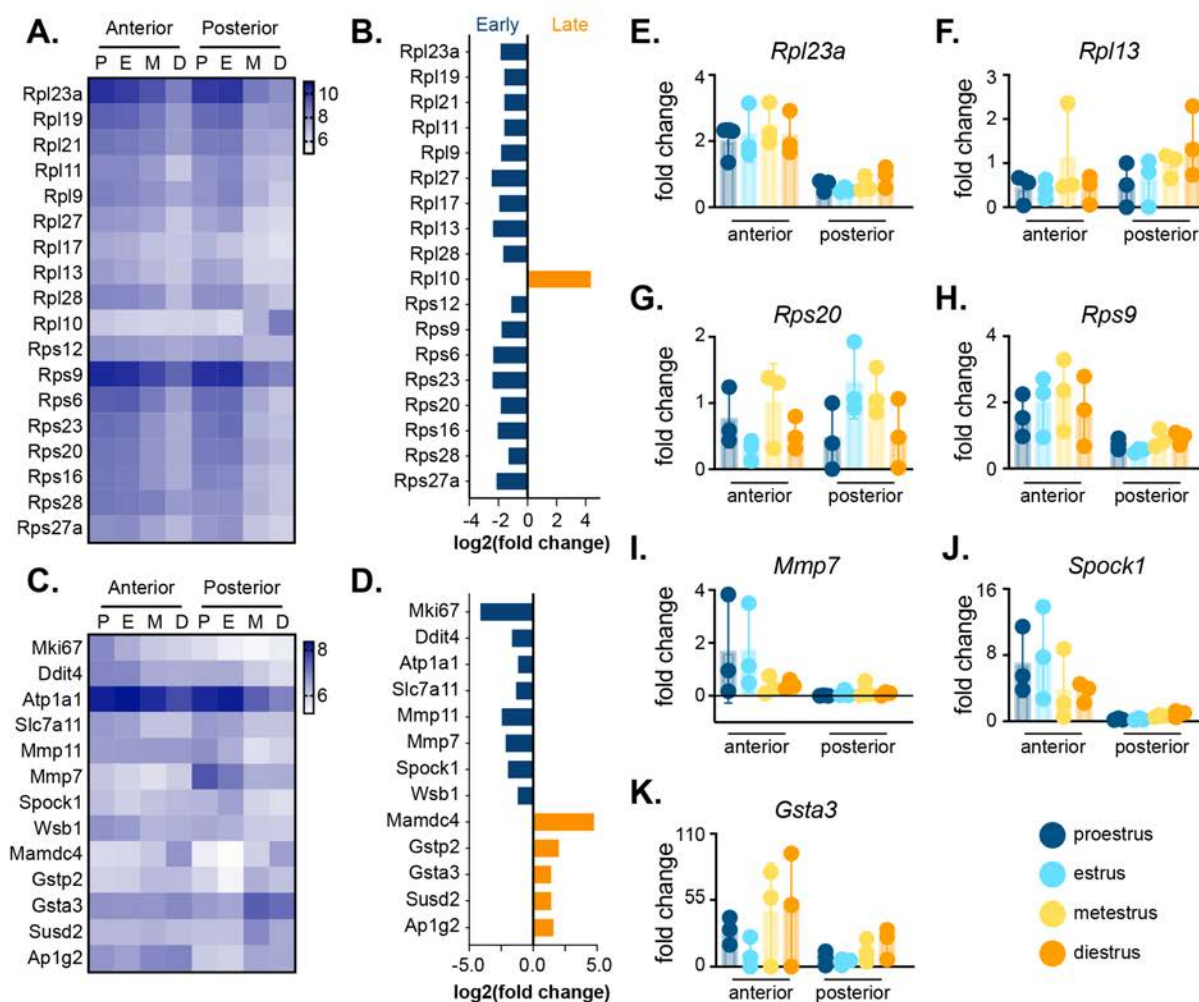
446 **Figure 3. The mouse oviduct transcriptome is remarkably stable across the estrous cycle.**

447 A) Heatmap depicting expression of ribosomal genes across the estrous cycle where rows

448 indicate genes and columns indicate the estrous cycle stage (P- proestrus, E- estrus, M-

449 metestrus, D- diestrus). B) The effect size (absolute value of the log2 fold change) of the

450 ribosomal genes was generally modest (under 2). C) Heatmap of other DEGs. D) These genes

451 also generally have modest but consistent effect sizes. E-K) qPCR histograms of select genes

452 from B and D along the anteroposterior axis at each estrous cycle stage. All heatmap scales use

453 DESeq2 variance stabilized counts.

454

455

456

457

458

17

Figure 4. The mouse oviduct displays robust transcriptional patterning along the anteroposterior axis. A) Heatmap showing expression dynamics of DEGs across the anterior and posterior, including cilia-related genes and complexes, solute carriers, transport ATPases, and calcium and potassium channels. Additional heatmaps of genes in developmental signaling pathways, including B) Wnt signaling, C) FGF signaling, D) Hox genes, and E) PCP signaling. F-R) qPCR histograms of select genes from A-E along the anteroposterior axis at each estrous cycle stage: anterior-enriched genes *Foxj1*, *Tmem231*, *Ift140*, *Ift57*, *Dnah9;* posterior-enriched genes *Atp1b1*, *Slc29a8*, *Msx2*, *Wnt7a*, *Wnt5a*; and other qPCR assayed genes *Prickle1*, *Vangl2*, *Pax8*.
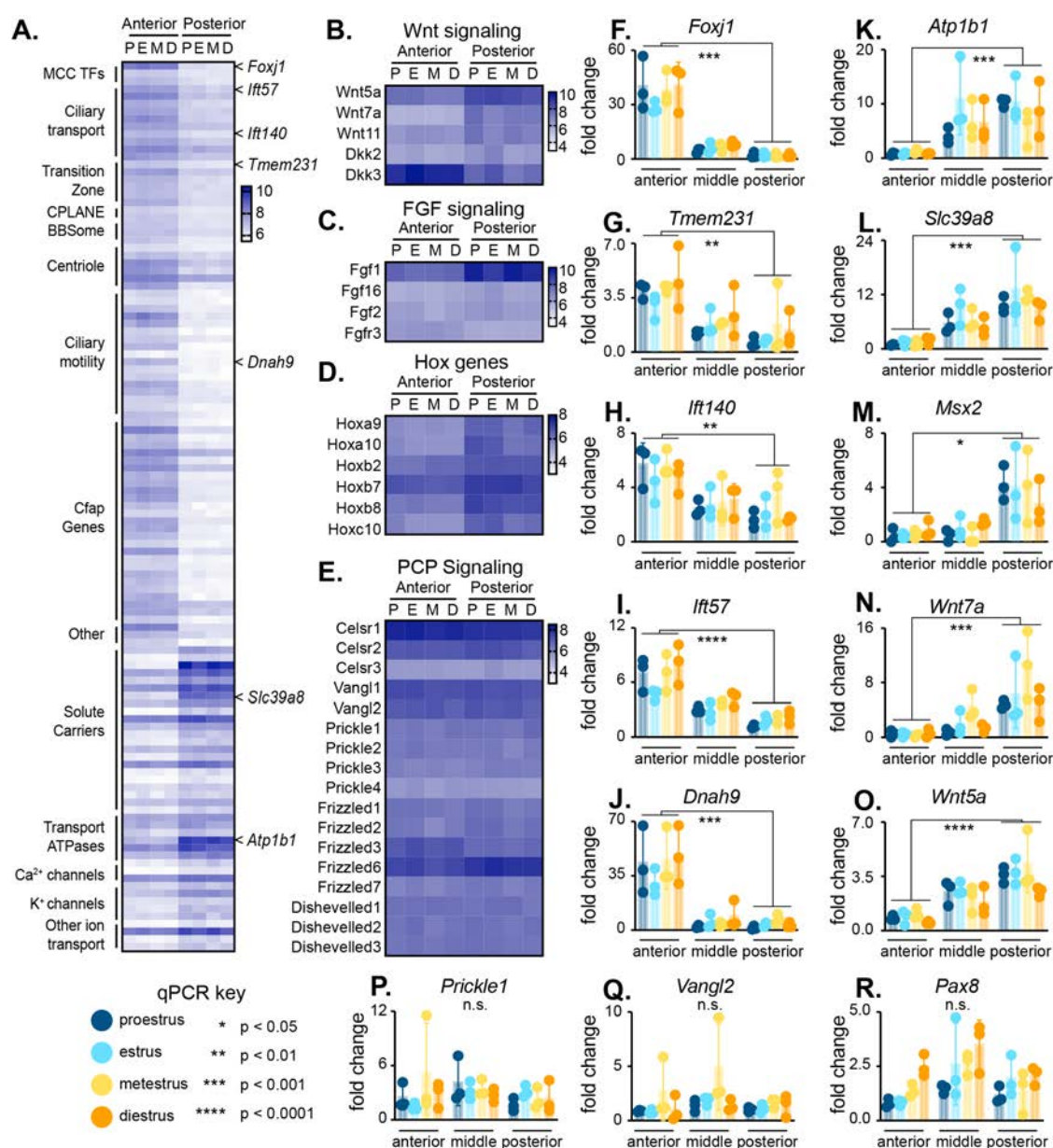
471 **Supplementary Figure 1. Significant GO terms associated with oviduct transcriptome**

472 **analysis.** Histograms depicting significant GO terms for A) early, B) late, C) anterior, and D)

473 posterior DEGs.
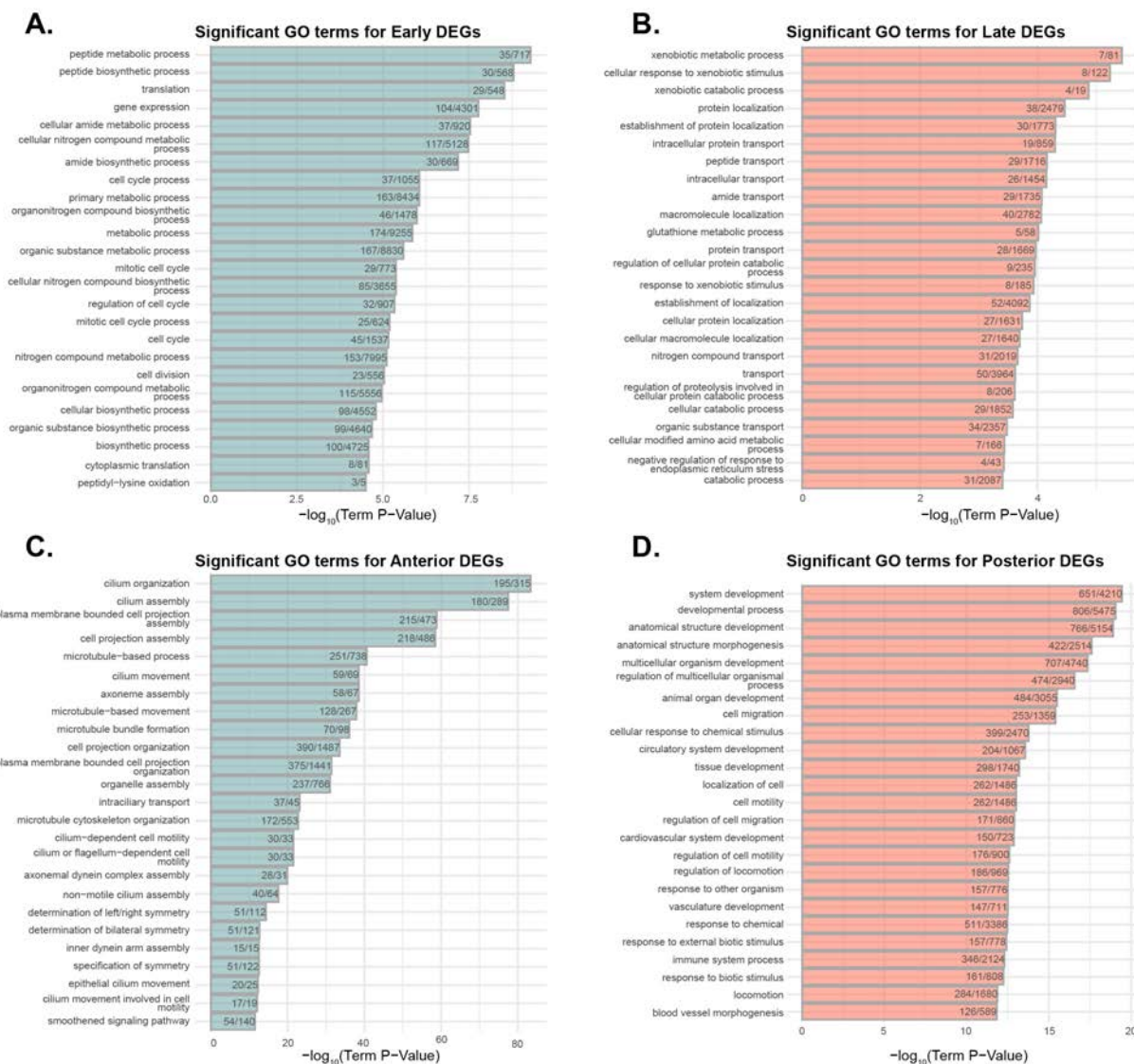
474
475

476 **Supplemental spreadsheet tabs:**

477 **S-1. Primers used for qPCR.**

478 **S-2. Description of the sample datasets used.**

479 Full DEG and GO term details are available in the Supplementary zip file for GEO accession

480 number GSE164718.

481

References

482 Agduhr, E., 1927. Studies on the structure and development of the bursa ovarica and the tuba
483 uterina in the Mouse. Acta Zoologica Stockholm 8, pp. 1-133.

485 Ajayi, A.F., Akhigbe, R.E., 2020. Staging of the estrous cycle and induction of estrus in
486 experimental rodents: an update. Fertil Res Pract 6, 5.

487 Alexa, A., Rahnenfuhrer, J, 2020. topGO: Enrichment Analysis for Gene Ontology, R package
488 version 2.40.0.

489 Andrews, S., FastQC. Babraham Bioinformatics, p.
490 https://www.bioinformatics.babraham.ac.uk/projects/fastqc/.

491 Barton, B.E., Herrera, G.G., Anamthathmakula, P., Rock, J.K., Willie, A., Harris, E.A.,
492 Takemaru, K.I., Winuthayanon, W., 2020. Roles of steroid hormones in oviductal function.
493 Reproduction 159, R125-r137.

494 Bauersachs, S., Rehfeld, S., Ulbrich, S.E., Mallok, S., Prelle, K., Wenigerkind, H., Einspanier,
495 R., Blum, H., Wolf, E., 2004. Monitoring gene expression changes in bovine oviduct epithelial
496 cells during the oestrous cycle. J Mol Endocrinol 32, 449-466.

497 Bray, N.L., Pimentel, H., Melsted, P., Pachter, L., 2016. Near-optimal probabilistic RNA-seq
498 quantification. Nat Biotechnol 34, 525-527.

499 Brenner, R.M., 1969. Renewal of oviduct cilia during the menstrual cycle of the rhesus monkey.
500 Fertil Steril 20, 599-611.

501 Brenner, R.M., West, N.B., 1975. Hormonal regulation of the reproductive tract in female
502 mammals. Annu Rev Physiol 37, 273-302.

503 Bronson, F.H., Hamilton, T.H., 1971. Concentrations of nucleic acids and protein in the mouse
504 oviduct during the oestrous cycle and after steroid replacement. J Reprod Fertil 25, 283-286.

505 Butler, M.T., Wallingford, J.B., 2017. Planar cell polarity in development and disease. Nat Rev
506 Mol Cell Biol 18, 375-388.

507 Bylander, A., Nutu, M., Wellander, R., Goksör, M., Billig, H., Larsson, D.G., 2010. Rapid
508 effects of progesterone on ciliary beat frequency in the mouse fallopian tube. Reprod Biol
509 Endocrinol 8, 48.

510 Cerny, K.L., Garrett, E., Walton, A.J., Anderson, L.H., Bridges, P.J., 2015. A transcriptomal
511 analysis of bovine oviductal epithelial cells collected during the follicular phase versus the luteal
512 phase of the estrous cycle. Reprod Biol Endocrinol 13, 84.

513 Coy, P., Garcia-Vazquez, F.A., Visconti, P.E., Aviles, M., 2012. Roles of the oviduct in
514 mammalian fertilization. Reproduction 144, 649-660.

515 Coy, P., Yanagimachi, R., 2015. The Common and Species-Specific Roles of Oviductal Proteins
516 in Mammalian Fertilization and Embryo Development. BioScience 65, 973-984.

517 Du, H., Taylor, H.S., 2015. The Role of Hox Genes in Female Reproductive Tract Development,
518 Adult Function, and Fertility. Cold Spring Harb Perspect Med 6, a023002.

519 Ewels, P., Magnusson, M., Lundin, S., Kaller, M., 2016. MultiQC: summarize analysis results
520 for multiple tools and samples in a single report. Bioinformatics 32, 3047-3048.

521 Ferenczy, A., Richart, R.M., Agate, F.J., Jr., Purkerson, M.L., Dempsey, E.W., 1972. Scanning
522 electron microscopy of the human fallopian tube. Science 175, 783-784.

523 Frankish, A., Diekhans, M., Ferreira, A.M., Johnson, R., Jungreis, I., Loveland, J., Mudge, J.M.,
524 Sisu, C., Wright, J., Armstrong, J., Barnes, I., Berry, A., Bignell, A., Carbonell Sala, S., Chrast,
525 J., Cunningham, F., Di Domenico, T., Donaldson, S., Fiddes, I.T., Garcia Giron, C., Gonzalez,
526 J.M., Grego, T., Hardy, M., Hourlier, T., Hunt, T., Izuogu, O.G., Lagarde, J., Martin, F.J.,
527 Martinez, L., Mohanan, S., Muir, P., Navarro, F.C.P., Parker, A., Pei, B., Pozo, F., Ruffier, M.,
528 Schmitt, B.M., Stapleton, E., Suner, M.M., Sycheva, I., Uszczynska-Ratajczak, B., Xu, J., Yates,
529 A., Zerbino, D., Zhang, Y., Aken, B., Choudhary, J.S., Gerstein, M., Guigo, R., Hubbard, T.J.P.,
530 Kellis, M., Paten, B., Reymond, A., Tress, M.L., Flicek, P., 2019. GENCODE reference
531 annotation for the human and mouse genomes. Nucleic Acids Res 47, D766-D773.

532 Gao, B., Song, H., Bishop, K., Elliot, G., Garrett, L., English, M.A., Andre, P., Robinson, J.,
533 Sood, R., Minami, Y., Economides, A.N., Yang, Y., 2011. Wnt signaling gradients establish

534   planar cell polarity by inducing Vangl2 phosphorylation through Ror2. Developmental cell 20,

535   163-176.

536   Garcia, G., 3rd, Raleigh, D.R., Reiter, J.F., 2018. How the Ciliary Membrane Is Organized

537   Inside-Out to Communicate Outside-In. Curr Biol 28, R421-R434.

538   Gentleman, R.C., Carey, V.J., Bates, D.M., Bolstad, B., Dettling, M., Dudoit, S., Ellis, B.,

539   Gautier, L., Ge, Y., Gentry, J., Hornik, K., Hothorn, T., Huber, W., Iacus, S., Irizarry, R., Leisch,

540   F., Li, C., Maechler, M., Rossini, A.J., Sawitzki, G., Smith, C., Smyth, G., Tierney, L., Yang,

541   J.Y., Zhang, J., 2004. Bioconductor: open software development for computational biology and

542   bioinformatics. Genome Biol 5, R80.

543   Ghosh, A., Syed, S.M., Tanwar, P.S., 2017. In vivo genetic cell lineage tracing reveals that

544   oviductal secretory cells self-renew and give rise to ciliated cells. Development (Cambridge,

545   England) 144, 3031-3041.

546   Gonella-Diaza, A.M., da Silva Andrade, S.C., Sponchiado, M., Pugliesi, G., Mesquita, F.S., Van

547   Hoeck, V., de Francisco Strefezzi, R., Gasparin, G.R., Coutinho, L.L., Binelli, M., 2017.

548   Oviductal transcriptional profiling of a bovine fertility model by next-generation sequencing.

549   Genom Data 13, 27-29.

550   Herrera, G.G.B., Lierz, S.L., Harris, E.A., Donoghue, L.J., Hewitt, S.C., Rodriguez, K.F.,

551   Jefferson, W.N., Lydon, J.P., DeMayo, F.J., Williams, C.J., Korach, K.S., Winuthayanon, W.,

552   2020. Oviductal Retention of Embryos in Female Mice Lacking Estrogen Receptor α in the

553   Isthmus and the Uterus. Endocrinology 161.

554   Hess, A.P., Talbi, S., Hamilton, A.E., Baston-Buest, D.M., Nyegaard, M., Irwin, J.C., Barragan,

555   F., Kruessel, J.S., Germeyer, A., Giudice, L.C., 2013. The human oviduct transcriptome reveals

556   an anti-inflammatory, anti-angiogenic, secretory and matrix-stable environment during embryo

557   transit. Reprod Biomed Online 27, 423-435.

558   Kessler, M., Hoffmann, K., Brinkmann, V., Thieck, O., Jackisch, S., Toelle, B., Berger, H.,

559   Mollenkopf, H.J., Mangler, M., Sehouli, J., Fotopoulou, C., Meyer, T.F., 2015. The Notch and

560   Wnt pathways regulate stemness and differentiation in human fallopian tube organoids. Nat

561   Commun 6, 8989.

562   Kim, J.M., Park, J.E., Yoo, I., Han, J., Kim, N., Lim, W.J., Cho, E.S., Choi, B., Choi, S., Kim,

563   T.H., Te Pas, M.F.W., Ka, H., Lee, K.T., 2018. Integrated transcriptomes throughout swine

564   oestrous cycle reveal dynamic changes in reproductive tissues interacting networks. Sci Rep 8,

565   5436.

566   Koyama, H., Shi, D., Fujimori, T., 2019. Biophysics in oviduct: Planar cell polarity, cilia,

567   epithelial fold and tube morphogenesis, egg dynamics. Biophys Physicobiol 16, 89-107.

568   Legendre, M., Zaragosi, L.E., Mitchison, H.M., 2020. Motile cilia and airway disease. Semin

569   Cell Dev Biol.

570   Lewis, M., Stracker, T.H., 2020. Transcriptional regulation of multiciliated cell differentiation.

571   Semin Cell Dev Biol.

572   Lohman, B.K., Weber, J.N., Bolnick, D.I., 2016. Evaluation of TagSeq, a reliable low-cost

573   alternative for RNAseq. Mol Ecol Resour 16, 1315-1321.

574   Love, M.I., Huber, W., Anders, S., 2014. Moderated estimation of fold change and dispersion for

575   RNA-seq data with DESeq2. Genome Biol 15, 550.

576   Maillo, V., de Frutos, C., O'Gaora, P., Forde, N., Burns, G.W., Spencer, T.E., Gutierrez-Adan,

577   A., Lonergan, P., Rizos, D., 2016. Spatial differences in gene expression in the bovine oviduct.

578   Reproduction 152, 37-46.

579   Matz, M., Tag-based RNAseq, pp. https://github.com/z0on/tag-based_RNAseq.

580   Meyer, E., Aglyamova, G.V., Matz, M.V., 2011. Profiling gene expression responses of coral

581   larvae (Acropora millepora) to elevated temperature and settlement inducers using a novel RNA-

582   Seq procedure. Mol Ecol 20, 3599-3616.

583   Novak, E., Everett, H., 1928. Cyclical and other variations in the tubal epithelium. American

584   Journal of Obstetrics and Gynecology 16, 499-530.

585   Ossipova, O., Kim, K., Sokol, S.Y., 2015. Planar polarization of Vangl2 in the vertebrate neural

586   plate is controlled by Wnt and Myosin II signaling. Biol Open 4, 722-730.

587   Patir, A., Fraser, A.M., Barnett, M.W., McTeir, L., Rainger, J., Davey, M.G., Freeman, T.C.,

588   2020. The transcriptional signature associated with human motile cilia. Scientific Reports 10,

589   10814.

590   Roberson, E.C., Tran, N.K., Konjikusic, M.J., Fitch, R.D., Gray, R.S., Wallingford, J.B., 2020. A

591   comparative study of the turnover of multiciliated cells in the mouse trachea, oviduct, and brain.

592   Dev Dyn 249, 898-905.

593   Rose, I.M., Bidarimath, M., Webster, A., Godwin, A.K., Flesken-Nikitin, A., Nikitin, A.Y.,

594   2020. WNT and inflammatory signaling distinguish human Fallopian tube epithelial cell

595   populations. Sci Rep 10, 9837.

596   Schmittgen, T.D., Livak, K.J., 2008. Analyzing real-time PCR data by the comparative C(T)

597   method. Nature protocols 3, 1101-1108.

598   Shi, D., Komatsu, K., Hirao, M., Toyooka, Y., Koyama, H., Tissir, F., Goffinet, A.M., Uemura,

599   T., Fujimori, T., 2014. Celsr1 is required for the generation of polarity at multiple levels of the

600   mouse oviduct. Development (Cambridge, England) 141, 4558-4568.

601   Shi, D., Komatsu, K., Uemura, T., Fujimori, T., 2011. Analysis of ciliary beat frequency and

602   ovum transport ability in the mouse oviduct. Genes Cells 16, 282-290.

603   Shi, D., Usami, F., Komatsu, K., Oka, S., Abe, T., Uemura, T., Fujimori, T., 2016. Dynamics of

604   planar cell polarity protein Vangl2 in the mouse oviduct epithelium. Mech Dev 141, 78-89.

605   Shirley, B., Reeder, R.L., 1996. Cyclic changes in the ampulla of the rat oviduct. J Exp Zool 276,

606   164-173.

607   Sisu, C., Muir, P., Frankish, A., Fiddes, I., Diekhans, M., Thybert, D., Odom, D.T., Flicek, P.,

608   Keane, T.M., Hubbard, T., Harrow, J., Gerstein, M., 2020. Transcriptional activity and strain-

609   specific history of mouse pseudogenes. Nat Commun 11, 3695.

610   Soneson, C., Love, M.I., Robinson, M.D., 2015. Differential analyses for RNA-seq: transcript-
611   level estimates improve gene-level inferences. F1000Res 4, 1521.

612   Sowamber, R., Nelson, O., Dodds, L., DeCastro, V., Paudel, I., Milea, A., Considine, M., Cope,
613   L., Pinto, A., Schlumbrecht, M., Slomovitz, B., Shaw, P.A., George, S.H.L., 2020. Integrative
614   Transcriptome Analyses of the Human Fallopian Tube: Fimbria and Ampulla-Site of Origin of
615   Serous Carcinoma of the Ovary. Cancers (Basel) 12.

616   Stewart, C.A., Behringer, R.R., 2012. Mouse oviduct development. Results Probl Cell Differ 55,
617   247-262.

618   Suarez, S.S., 2016. Mammalian sperm interactions with the female reproductive tract. Cell
619   Tissue Res 363, 185-194.

620   Talbot, P., Geiske, C., Knoll, M., 1999. Oocyte pickup by the mammalian oviduct. Mol Biol Cell
621   10, 5-8.

622   Verhage, H., Abel Jr, J., Tietz Jr, W., Barrau, M., 1973. Development and maintenance of the
623   oviductal epithelium during the estrous cycle in the bitch. Biology of reproduction 9, 460-474.

624   Winuthayanon, W., Bernhardt, M.L., Padilla-Banks, E., Myers, P.H., Edin, M.L., Lih, F.B.,
625   Hewitt, S.C., Korach, K.S., Williams, C.J., 2015. Oviductal estrogen receptor alpha signaling
626   prevents protease-mediated embryo death. Elife 4, e10453.

627   Yamanouchi, H., Umezu, T., Tomooka, Y., 2010. Reconstruction of oviduct and demonstration
628   of epithelial fate determination in mice. Biology of reproduction 82, 528-533.

629   Zeisel, A., Yitzhaky, A., Bossel Ben-Moshe, N., Domany, E., 2013. An accessible database for
630   mouse and human whole transcriptome qPCR primers. Bioinformatics 29, 1355-1356.
631
632

Table S-1

Gene	Sequence
Rpl23a	F: 5' - AGGCAGCCAAAATATCCTCG - 3'
	R: 5' - TTCTTCATGGCTGACTCCGT - 3'
Rps9	F: 5' - GCTAGACGAGAAGGATCCCC – 3'
	R: 5' - ATCCAGCTTCATCTTGCCCT – 3
Rpl13	F: 5' - TACTGAAGCCCCACTTCCAC - 3'
	R: 5' - CGGACCTTGGTGTGGTATCT - 3'
Rps20	F: 5' - GAACAAGTCGGTCAGGAAGC - 3'
	R: 5' - CTCTGATCAAGTCCGCACAA - 3'
Mmp7	F: 5' - CCTAGGCGGAGATGCTCACT -3'
	R: 5' - GAGAGTGGCCAAATTCATGG - 3'
Spock1	F: 5'- CTGAAGCCCAAAGCAGAGAA - 3'
	R: 5' - CTCATGAAGAGCCCCGAAC - 3'
Gsta3	F: 5' - GATTTAGACTCCAAGCGGCA - 3'
	R: 5' - TTCCCCTGCCATCAAAGTAA - 3'
Foxj1	F: 5'- TGTGGATCTTACAGTCCATGGC -3'
	R: 5'- TCTCATCAAAGTCCAGGCTGTC -3'
Tmem231	F: 5'- AACAGAAGCAGCCACTGAGC -3'
	R: 5'- AACAATGTGGGTGAGGTCGT -3'
Ift140	F: 5'- ATTCCTGGCAGTCGCATCTA -3'
	R: 5'- GAAGTGGCCTGGAAAGACCT -3'
Ift57	F: 5'- GCGGAATGGAGCCTAGAAGT -3'
	R: 5'- CTTTTGTGCTGGTGCATTTG -3'
Dnah9	F: 5'- TGTGAACGCATGAACATCCT -3'
	R: 5'- TTCCATCTCACTGGTCATGGT -3'
Msx2	F: 5'- AGCTGAAAATGGCTGCCAAG -3'
	R: 5'- TAGGATGCGCCGTATATGGATG -3'
Wnt7a	F: 5'- GCCTGGACGAGTGTCAGTTT -3'
	R: 5'- AATCGCATAGGTGAAGGCAG -3'
Wnt5a	F: 5'- CACGTTTTTCTCCTTCGCC -3'
	R: 5'- AGTTGGCTGCAGAGAGGCT -3'
Slc39a8	F: 5'- GGCCAGCTGCACTTCAAC -3'
	R: 5'- GCAGATGGCAGAGAAGTTCG -3'
Atp1b1	F: 5'- GAAGCCCTGCATCATTATCAA -3'
	R: 5'- GAACAGGCAGGACATTTGGA -3'
Prickle1	F: 5'- GTGGCTGCTTCGAGTCTCTC -3'
	R: 5'- TCGTAGGTCATCTGTGCGTG -3'
Vangl2	F: 5'- TACTACGAGGAAGCCGAGCA -3'
	R: 5'- CTTCCTGCAGCCGCTTAAT -3'
Pax8	F: 5' – ACAGGGCAGCTATGCCTCTT - 3'
	R: 5' – GCTGTAGGCATTGCCAGAAT - 3'
Hprt	F: 5' – CATAACCTGGTTCATCATCGC - 3'
	R: 5' – TCCTCCTCAGACCGCTTTT - 3'
Dolk	F: 5' – CAGTGTGGGACCGATACTCCT - 3'
	R: 5' – CCAAGCAAAGGCATGACCA - 3'
Sra1	F: 5' – ACGACCCGCCACAATTCTC - 3'
	R: 5' – CTGGAAGCCTTACTTGAAGGAG - 3'

	Table S-2										
ID	Sample	Location	Stage	Phase	Location_Phase	# Raw reads	# Deduped	# Aligned	% Align	GEO Fastq file	GEO kallisto counts file
S1	Proes_Ant_B1	Anterior	Proestrus	Early	Anterior_Early	2,669,590	1,392,774	1,038,851	74.6%	Proes_Ant_B1_R1.fastq.gz	Proes_Ant_B1_kallisto_counts.tsv
S2	Proes_Ant_B2	Anterior	Proestrus	Early	Anterior_Early	2,903,086	1,583,735	1,184,664	74.8%	Proes_Ant_B2_R1.fastq.gz	Proes_Ant_B2_kallisto_counts.tsv
S3	Proes_Post_B1	Posterior	Proestrus	Early	Posterior_Early	3,820,771	1,809,899	1,358,747	75.1%	Proes_Post_B1_R1.fastq.gz	Proes_Post_B1_kallisto_counts.tsv
S4	Proes_Post_B2	Posterior	Proestrus	Early	Posterior_Early	2,542,319	1,258,262	936,809	74.5%	Proes_Post_B2_R1.fastq.gz	Proes_Post_B2_kallisto_counts.tsv
S5	Es_Ant_B1	Anterior	Estrus	Early	Anterior_Early	3,859,515	2,015,223	1,524,157	75.6%	Es_Ant_B1_R1.fastq.gz	Es_Ant_B1_kallisto_counts.tsv
S6	Es_Ant_B2	Anterior	Estrus	Early	Anterior_Early	4,976,661	2,393,539	1,803,496	75.3%	Es_Ant_B2_R1.fastq.gz	Es_Ant_B2_kallisto_counts.tsv
S7	Es_Post_B1	Posterior	Estrus	Early	Posterior_Early	3,051,253	1,508,916	1,166,422	77.3%	Es_Post_B1_R1.fastq.gz	Es_Post_B1_kallisto_counts.tsv
S8	Es_Post_B2	Posterior	Estrus	Early	Posterior_Early	1,486,318	792,559	589,353	74.4%	Es_Post_B2_R1.fastq.gz	Es_Post_B2_kallisto_counts.tsv
S9	Metes_Ant_B1	Anterior	Metestrus	Late	Anterior_Late	1,509,395	896,284	696,932	77.8%	Metes_Ant_B1_R1.fastq.gz	Metes_Ant_B1_kallisto_counts.tsv
S10	Metes_Ant_B2	Anterior	Metestrus	Late	Anterior_Late	1,742,088	1,000,503	771,609	77.1%	Metes_Ant_B2_R1.fastq.gz	Metes_Ant_B2_kallisto_counts.tsv
S11	Metes_Post_B1	Posterior	Metestrus	Late	Posterior_Late	3,034,943	1,266,394	989,728	78.2%	Metes_Post_B1_R1.fastq.gz	Metes_Post_B1_kallisto_counts.tsv
S12	Metes_Post_B2	Posterior	Metestrus	Late	Posterior_Late	4,033,746	1,918,652	1,484,995	77.4%	Metes_Post_B2_R1.fastq.gz	Metes_Post_B2_kallisto_counts.tsv
S13	Dies_Ant_B1	Anterior	Diestrus	Late	Anterior_Late	4,403,124	2,067,053	1,605,618	77.7%	Dies_Ant_B1_R1.fastq.gz	Dies_Ant_B1_kallisto_counts.tsv
S14	Dies_Ant_B2	Anterior	Diestrus	Late	Anterior_Late	4,161,010	1,439,043	1,088,609	75.6%	Dies_Ant_B2_R1.fastq.gz	Dies_Ant_B2_kallisto_counts.tsv
S15	Dies_Post_B1	Posterior	Diestrus	Late	Posterior_Late	2,131,914	946,725	726,724	76.8%	Dies_Post_B1_R1.fastq.gz	Dies_Post_B1_kallisto_counts.tsv
S16	Dies_Post_B2	Posterior	Diestrus	Late	Posterior_Late	1,522,405	721,007	572,923	79.5%	Dies_Post_B2_R1.fastq.gz	Dies_Post_B2_kallisto_counts.tsv